

DSMS Telecommunications Link  
Design Handbook

---


# 106, Rev. A


## Solar Corona and Solar Wind Effects

Released October 21, 2005


---

Authors:

  
C. Ho 10/5/05  
Date

  
D. Morabito 10/5/05  
Date

Approved by:

  
Timothy T. Pham 10/6/05  
DSN Chief System Engineer Date

Released by:

Signature on file at  
DSMS Library 10/21/2005  
DSMS Document Release Date

### ***Change Log***

<b>Rev</b>	<b>Issue Date</b>	<b>Affected Paragraphs</b>	<b>Change Summary</b>
Initial	8/10/2005	All	Initial Release
A	10/7/2005	2.1.1, 2.1.3	Corrected units of Equation 4, Added attribution for Figures 2 and 4.

### ***Note to Readers***

There are two sets of document histories in the 810-005 document that are reflected in the header at the top of the page. First, the overall document is periodically released as a revision when major changes affect a majority of the modules. For example, this document is part of Revision E. Second, the individual modules also change, starting as the initial issue that has no revision letter. When a module is changed, a change letter is appended to the module number on the second line of the header and a summary of the changes is entered in the module's change log.

## ***Contents***

<u><b>Paragraph</b></u>	<u><b>Page</b></u>
1 Introduction .....	4
1.1 Purpose .....	4
1.2 Scope .....	4
2 General Information.....	4
2.1 Effects in Homogeneous Region of the Solar Wind.....	6
2.1.1 Group Delay.....	6
2.1.2 Dispersion .....	8
2.1.3 Faraday Rotation .....	9
2.1.4 Absorption .....	11
2.2 Solar Effects in Inhomogeneous Plasma.....	11
2.2.1 Intensity Scintillation .....	11
2.2.1.1 Measurements.....	12
2.2.1.2 Data Reduction Technique .....	12
2.2.1.3 Discussion of the X-band Scintillation Measurements .....	12
2.2.1.4 Discussion of the Ka-band Scintillation Measurements .....	13
2.2.1.5 Scintillation Model.....	14
2.2.2 Spectral Broadening .....	15
2.3 Communications Strategies.....	16
Appendix A, References .....	17

## ***Illustrations***

<u><b>Figure</b></u>	<u><b>Page</b></u>
1. Geometric Relationships for Calculating Solar Effects.....	5
2. Slant Total Electron Content (STEC) as a Function of Sun-Earth-Probe and Earth-Sun-Probe Angles.....	7
3. Comparison of Model with Representative Data from Several Solar Occultations..	8
4. S-band Coronal Faraday Rotation (Helios-1 Spacecraft, Day 241, 1975).....	10
5. X-band Scintillation Index vs. Solar Elongation Angle. ....	13
6. Ka-band Scintillation Index vs. Solar Elongation Angle.....	14

## ***1 Introduction***

### ***1.1 Purpose***

This module describes the effects of the solar corona and solar wind on Deep Space Network (DSN) telecommunications links. This will enable a telecommunications engineer to predict radio metric and radio science data performance of a signal at S, X and Ka bands when passing through the solar corona and solar wind.

### ***1.2 Scope***

This module discusses the effects of the solar corona and solar wind on DSN telecommunications links. The telecommunications performance in the absence of these effects and in the absence of weather effects is described in the telecommunications interfaces module for each antenna type (modules 101, 102, 103, and 104). Weather effects are discussed in module 105, Atmospheric and Environmental Effects. Module 105 also provides information on the effect of solar radiation on the operating system noise temperature of the antennas.

## ***2 General Information***

The solar corona and solar wind are the result of high density and strongly turbulent ionized gases (plasma) being ejected from the Sun. These ionized particles stream from the Sun at speeds on the order of 400 km/s and form the solar wind. The solar wind is not uniform and is accompanied by significant fluctuations in the solar magnetic field. Solar wind plasma density decreases with radial distance and becomes largely homogeneous when the distance from the Sun exceeds 4 solar radii. Within 4 solar radii, turbulence and irregularities are much greater and the plasma must be considered inhomogeneous. When radio frequency (RF) waves pass through these regions, the signals suffer severe degradation of their amplitude, frequency and phase.

Estimation of solar effects is complicated by the solar cycle that places an overlay of solar event frequency on top of the normal solar activity. Such events include coronal mass ejections, and an increase in the number of streamers. During the low periods of the solar cycle, events are less frequent and generally confined to the Sun's equatorial region. During periods of high solar activity, events are much more frequent and may occur at any place on the Sun's surface. Disentangling solar latitude dependence and solar activity dependence in each conjunction data set is difficult. In addition, many times the spacecraft ingress and egress scintillation profile curves are asymmetric and take on a different character depending on solar conditions. A chart predicting solar activity is shown in module 105.

Figure 1 illustrates the regions of the Sun and geometric relationships used in this module. The closest distance between the signal path and the Sun is  $a$ , the Solar Elongation

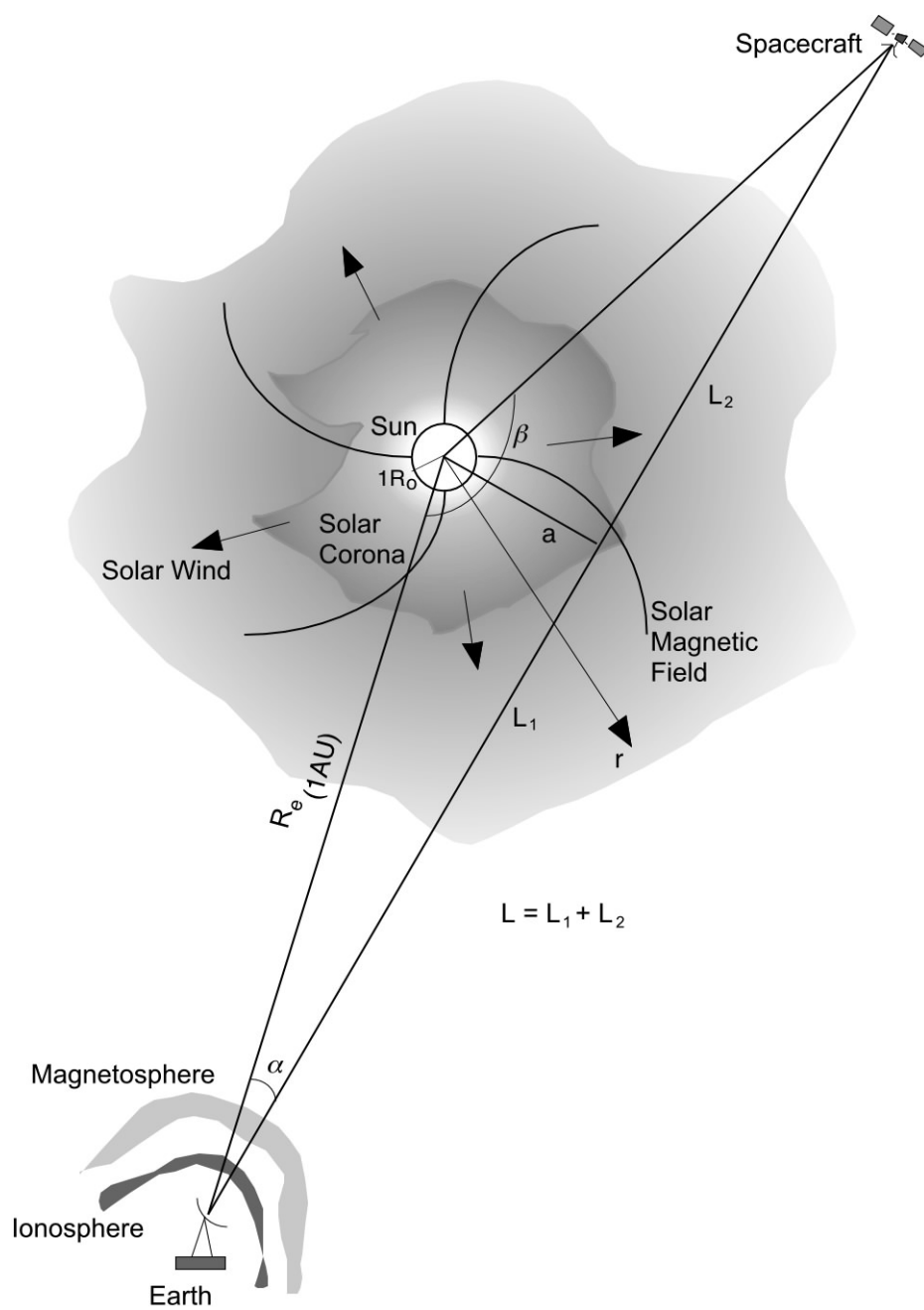


Figure 1. Geometric Relationships for Calculating Solar Effects

Angle or Sun-Earth-probe (SEP) angle is  $\alpha$  (1 solar radius in  $a = 0.25^\circ$  in  $\alpha$ ), the spacecraft-Sun-Earth angle is  $\beta$ , and the signal path length between spacecraft and the Earth station is  $L$ . The figure also shows the Earth's ionosphere and magnetosphere that have a relatively low plasma density.

## 2.1 *Effects in Homogeneous Region of the Solar Wind*

As a plasma medium, the homogeneous region of the solar wind has the following basic effects on radio wave signals.

### 2.1.1 *Group Delay*

Group delay is the extra time delay due to the presence of an ionized medium in the propagation path. It is a function only of the slant total electron contents (*STEC*) along the path and the radio-wave frequency. It is defined as

$$\Delta T = \frac{1.3446 \times 10^{-19}}{f^2} \times \int_{L_{S/C}} N_e dl \quad (1)$$

where

$\Delta T$  = the group delay ( $\mu s$ )

$f$  = the radio-wave frequency (GHz)

$\int_{L_{S/C}} N_e dl$  the *STEC* along the entire path,  $L$ , from earth station to spacecraft (see Figure 1).

$N_e$  is solar wind electron density, a function only of radial distance. At low heliospheric latitude and equatorial regions, it can be modeled as [1]:

$$N_e(a) = 2.21 \times 10^{14} \left( \frac{a}{R_0} \right)^{-6} + 1.55 \times 10^{12} \left( \frac{a}{R_0} \right)^{-2.3} \quad (2)$$

where

$R_0$  = solar radius ( $6.96 \times 10^8$  m)

$a$  = radial distance, m.

This model is one of several postulated for  $N_e(a)$ , the primary difference between the models being the exponent of the second term. For example, the Muhleman-Anderson model [2] uses an exponent ranging from  $-2.04$  to  $-2.08$ .

Finally, the integration along the ray path is a function of angles  $\alpha$  and  $\beta$  that uniquely define the path,  $L$  (see Figure 1).

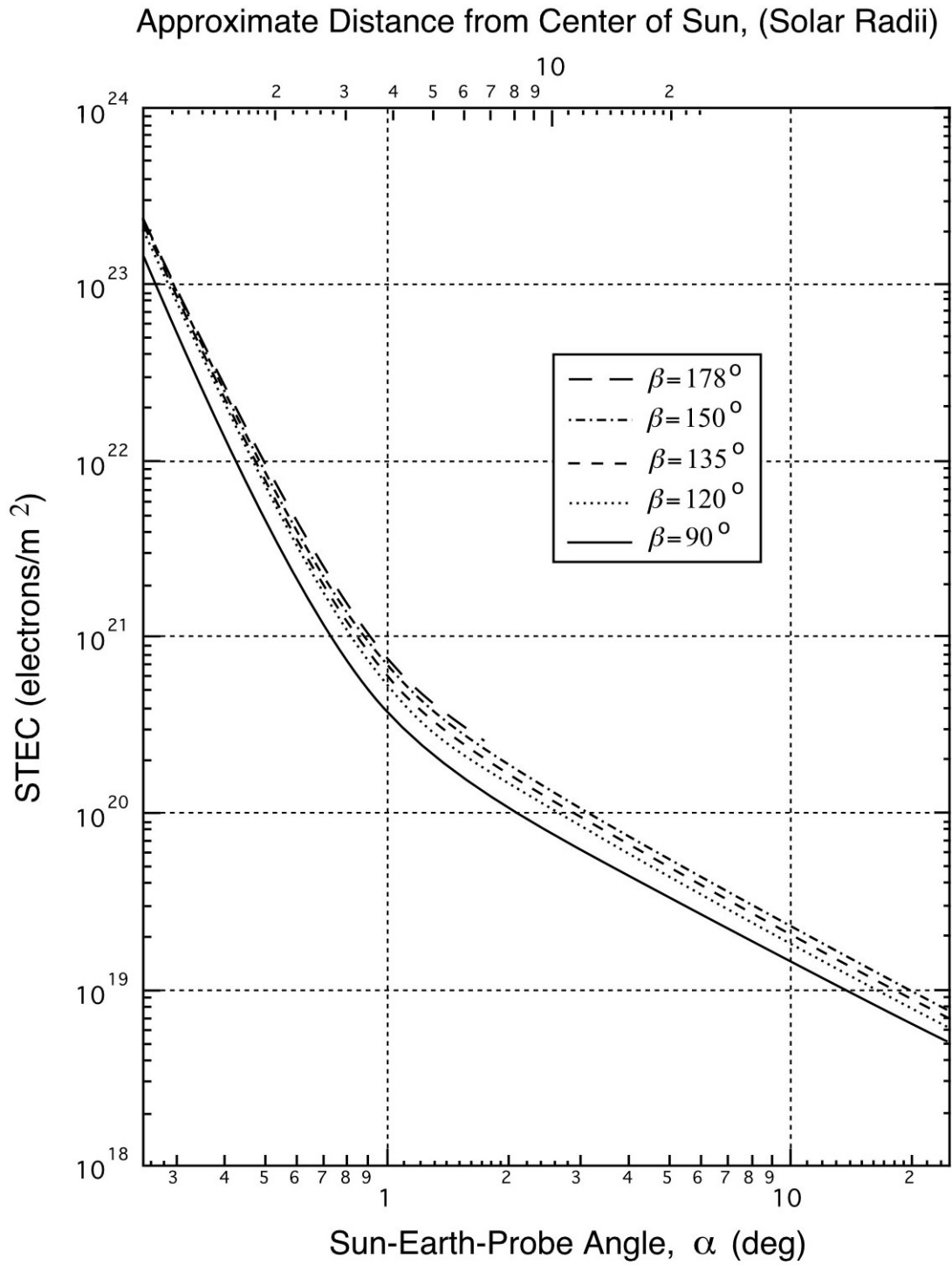


Figure 2. Slant Total Electron Content (STEC) as a Function of Sun-Earth-Probe and Earth-Sun-Probe Angles.

Figure 2 can be used to determine the approximate value of  $STEC$  as a function of Sun-Earth-Probe Angle,  $\alpha$ , or distance from the center of the sun in solar radii, for values of  $\beta$  between  $90^\circ$  and  $178^\circ$ . For example, if a ray path passes near the Sun such that  $\alpha$  and  $\beta$  are  $1.5^\circ$  and  $150^\circ$ , the  $STEC$  will be approximately  $3 \times 10^{20}$  electrons/m<sup>2</sup>. Substituting this value in equation (1) provides a  $\Delta T = 7.5 \mu s$  for an S band (2.3 GHz) signal and  $0.6 \mu s$  for an X band (8.42 GHz) signal. Figure 3 illustrates this model as applied to an S-band Uplink and X-band downlink signal along with data from the Viking [2] and Ulysses [3] missions that used these frequencies for their telecommunications links.

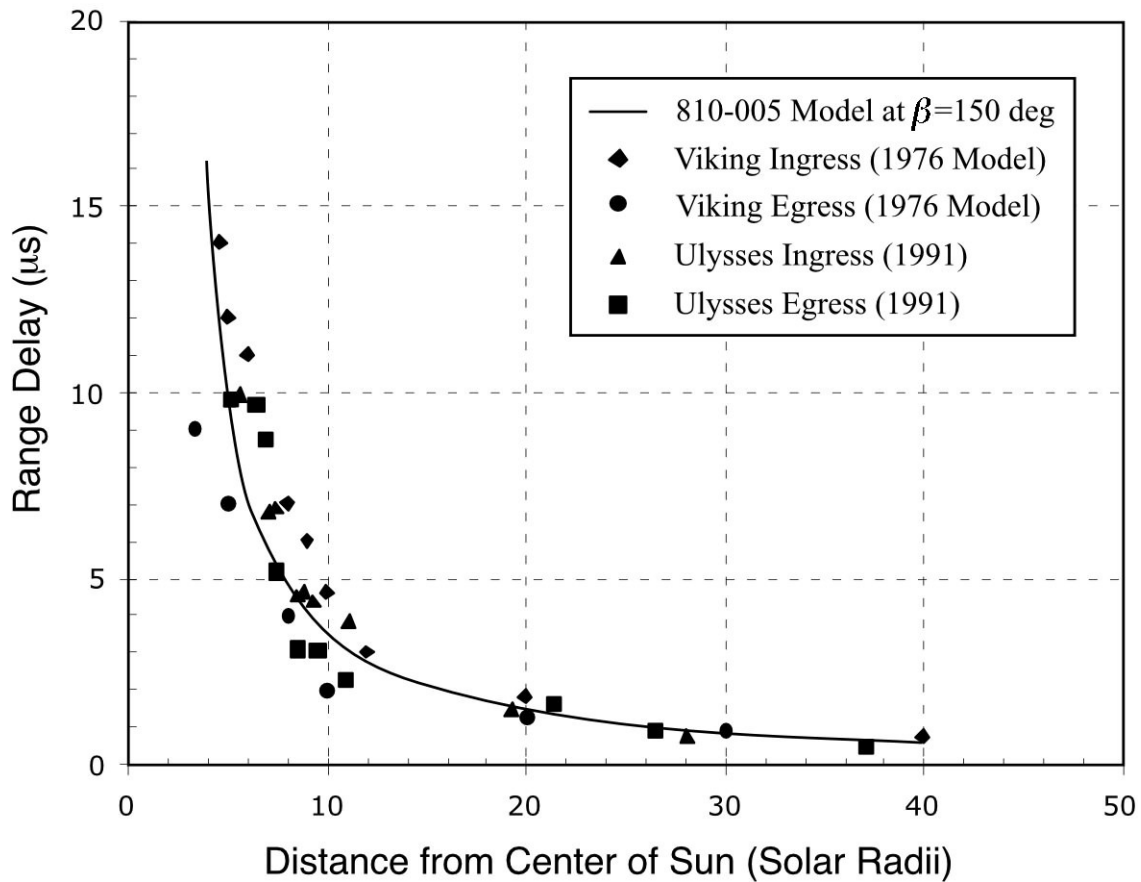


Figure 3. Comparison of Model with Representative Data from Several Solar Occultations.

### 2.1.2 Dispersion

Because group velocity is a function of the radio signal frequency, a dispersive phenomenon will occur when a broad band of frequency signals pass through the solar wind.



Differentiating the group delay  $\Delta T$  in (1) and scaling to appropriate units yields the following relation

$$\frac{\Delta T}{\Delta f} = \frac{2.69 \times 10^{-19}}{f^3} \int_{L_{S/C}} N_e dl = \frac{2.69 \times 10^{-19}}{f^3} \times STEC. \quad (3)$$

where

$$\frac{\Delta T}{\Delta f} = \text{dispersion (ns/MHz)}$$

Using the  $STEC$  value derived above for an SEP angle of  $1.5^\circ$  and  $\beta = 150^\circ$ , we find  $\Delta T/\Delta f = 0.135$  ns/MHz for X band frequencies.

### 2.1.3 *Faraday Rotation*

An RF wave traversing the solar corona at an angle  $\theta_B$  with respect to the Sun's magnetic field  $B$  (quasi-longitudinal) will rotate its polarization plane. The total rotation  $\phi$  in radians is proportional to the product of the electron density and the magnetic field component along the path from the probe to the observer and is given to a very good approximation by

$$\phi = \frac{2.36 \times 10^{-17}}{f^2} \int_{L_{S/C}} N_e \vec{B} \cos \theta_B dl, \text{ rad} \quad (4)$$

where

$$\begin{aligned} f &= \text{signal frequency, MHz} \\ B &= \text{magnetic field magnitude, nT} \\ N_e &= \text{solar wind electron density, m}^{-3}. \end{aligned}$$

Thus, a large Faraday rotation could result from either a high electron density or a large net longitudinal field component. On the other hand, high electron densities and strong magnetic fields could produce no net Faraday rotation if the field orientations are such as to cancel out in the integral.

The observed Faraday rotation is due to the effects of both the solar corona and the plasma in the Earth's ionosphere however, the ionospheric contribution is usually negligible when the ray path passes within 10 solar radii of the sun. An example of S-band Faraday rotation as measured from two Earth stations during the second of two solar occultations by the Helios-1 spacecraft is shown in Figure 4 [4].

The change in polarization angle due to Faraday rotation can be measured at stations that are capable of receiving simultaneous RCP and LCP signals provided the spacecraft radiates significant energy in each circular polarization (or employs a linearly polarized signal). The 70-m stations presently have the capability for simultaneous RCP and LCP reception at S- and X-bands, and several of the BWG stations have this capability at X-band.

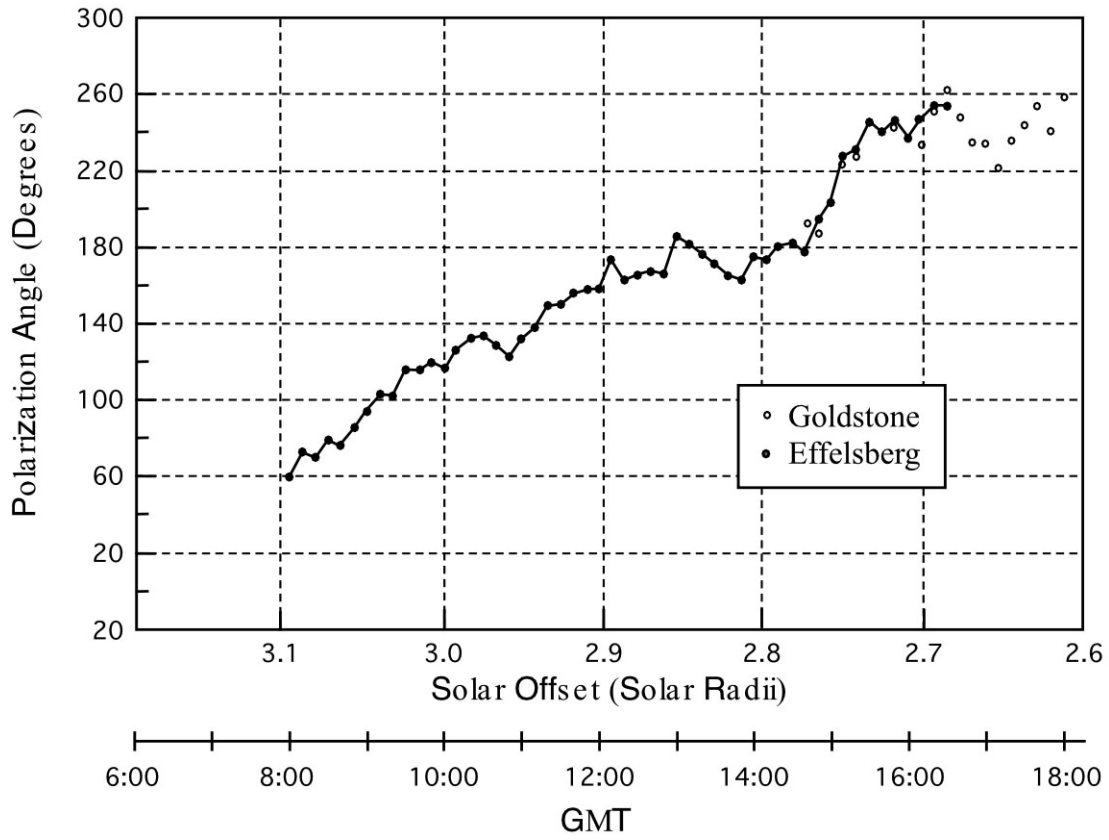


Figure 4. S-band Coronal Faraday Rotation (Helios-1 Spacecraft, Day 241, 1975).

The polarization angle is related to the phases of the received signals by

$$\alpha_{s,x} = \frac{\phi_{s,x}^{RCP} - \phi_{s,x}^{LCP}}{2} \quad (5)$$

where

$\phi_{s,x}$  = polarization angle at the received frequency

$\phi_{s,x}^{RCP}$  and  $\phi_{s,x}^{LCP}$  are the phases of the S- or X-band RCP and LCP components.

The factor of one-half is necessary because Faraday rotation has equal but opposite effects on the phase of each circular polarization. That is, if it retards the phase of the RCP signal, it will advance the phase of the LCP signal and vice-versa.

#### 2.1.4 *Absorption*

The absorption effect of solar wind plasma in the microwave bands,  $L_a$ , is very small and is given by

$$L_a = \frac{1.15 \times 10^{-21}}{f^2} \int_{L_{S/C}} N_e \nu dl, \text{ dB} \quad (6)$$

where

- $N_e$  = solar wind electron density,  $\text{m}^{-3}$
- $\nu$  = plasma collision frequency, Hz, (a function of temperature)
- $f$  = signal frequency, GHz

For a 2.3 GHz signal and a path length of  $3 \times 10^8$  km, the total absorption will be only 0.01 dB and is negligible.

## 2.2 *Solar Effects in Inhomogeneous Plasma*

The solar corona and near-sun solar wind are an inhomogeneous plasma medium because of strong turbulence and irregularities—especially within 4 solar radii. In addition to the effects mentioned in Section 2.1, radio signals will experience intensity scintillations, spectral broadening, and phase scintillations. The first two of these are discussed below. Phase scintillation will be discussed in a later revision of this module.

### 2.2.1 *Intensity Scintillation*

RF signals passing through solar corona are scattered by turbulence within the Fresnel Zone of the signal. The Fresnel Zone size can be approximated by  $\sqrt{\lambda L_1}$ , where  $L_1$  is the distance to the irregularity, usually assumed to be 1 AU. Irregularities within this region are classified as *small-scale* irregularities. Rapid amplitude changes around the average signal level will occur due to wave ray path changes and phase shifting as different portions of the wave front are affected to differing degrees. This is observed as instantaneous degradations to the received signal to noise ratio (SNR). The intensity scintillations can be described using a scintillation index,  $m$ , that is defined as the RMS of the signal intensity fluctuations divided by their mean intensity. As the intensity of the scintillations increase, their RMS value approaches the mean and the index becomes saturated at 1.

The scintillation index can be calculated from a measurement time series of signal strength, as the ratio of the RMS of the received power fluctuations relative to the mean power, over the observation interval. This parameter is only sensitive to characterizing the strength of small-scale charged particle density irregularities. In the regime of *weak scintillation*, ( $0 < m < 0.5$ ), the RMS of the fluctuations is small relative to the mean intensity. In the regime of strong scintillation, the RMS of the fluctuations will be comparable to the mean intensity. As the SEP angle decreases, the scintillation index for a point source will increase until saturation occurs,

and then there will not be any further increase in  $m$  as the SEP angle decreases. Saturation is usually reached at an SEP angle  $\sim 1.2^\circ$  for X-band and  $\sim 0.6^\circ$  for Ka-band. However, the time scale of the fluctuations may become shorter as the SEP angle decreases further in the regime of saturation.

For spacecraft telemetry, frame errors have been observed to significantly increase when the scintillation index reaches values of 0.3 and above [5]. When the scintillation index is less than 0.3, few frame errors have been observed provided sufficient margin was available in both the carrier and data channels. This transition point where telemetry frame errors significantly increase occurs near  $2.3^\circ$  for X-band and is expected to occur near  $\sim 1^\circ$  for Ka-band [5]. Flight projects and design engineers can use such information in the planning of solar conjunction operational scenarios.

#### **2.2.1.1      *Measurements***

Figures 5 and 6 illustrate the values of the X-band and Ka-band scintillation indices that were measured from solar conjunction experiments of interplanetary spacecraft missions along with solid lines depicting the theoretical model curves described in Reference [6]. The missions included Mars Global Surveyor (MGS) in 1998 [7], Stardust in 2000 (X-band only), Cassini in 2000 [8], Deep Space 1 in 2000 [9], and Cassini in 2001. The Ka-band data for the 2001 Cassini conjunction are broken into two subsets with one representing the egress on day 158 and the second representing the data from all other tracks in 2001.

#### **2.2.1.2      *Data Reduction Technique***

Most of the X-band data points from the MGS 1998 conjunction were from Block V Receiver (BVR) closed-loop data while most of the data points (X-band and Ka-band) from the other conjunctions were estimated using a software phase-locked-loop (PLL) program run on open-loop receiver sampled data recorded during the passes. The PLL algorithm used on the open-loop data samples acquired during strong scintillation or saturation results in lost fluctuation information due to the filtering effects of the PLL when the signal SNR gets too low during the deep fading. This results in depressed estimates of scintillation index. Therefore, the X-band scintillation data points with  $SEP < 1^\circ$  were evaluated using an alternative approach. The histogram of the open-loop amplitude samples were fit to a Rician distribution function, solving for the Rician mean and sigma parameters, as well as a scale factor. These were then converted to scintillation index using appropriate formulation [10]. This approach appears to be very reasonable, as the resulting scintillation index values lie near unity, as expected in this region of small solar impact distance.

#### **2.2.1.3      *Discussion of the X-band Scintillation Measurements***

The scintillation index is reduced when the signal traverses regions of less dense and less turbulent plasma, such as coronal holes. Most of the MGS 1998 X-band ingress points lie below the theoretical model in Figure 5 as the spacecraft signal was propagating through a coronal hole. The MGS 1998 egress measurements lie above and below the theoretical model, with the data points lying above the model appearing to be correlated with solar activity [7].

A significant increase in X-band scintillation index was observed during a Cassini solar conjunction pass in May 2000. This event occurred during a pass conducted at an SEP angle of  $1.8^\circ$  during egress, while in the X-band weak scintillation realm ( $m < 1$ ). Hence, density-induced changes were detectable in which  $m$  increased from its background level of  $m \sim 0.4$  up to  $m \sim 0.8$ . Two data points from this pass are plotted in Figure 5. This change in X-band scintillation index during a single pass is consistent with the overall scatter of all the measurements about the model for  $\text{SEP} < 2^\circ$ , suggesting that such variability may contribute to the scatter seen in other measurements.

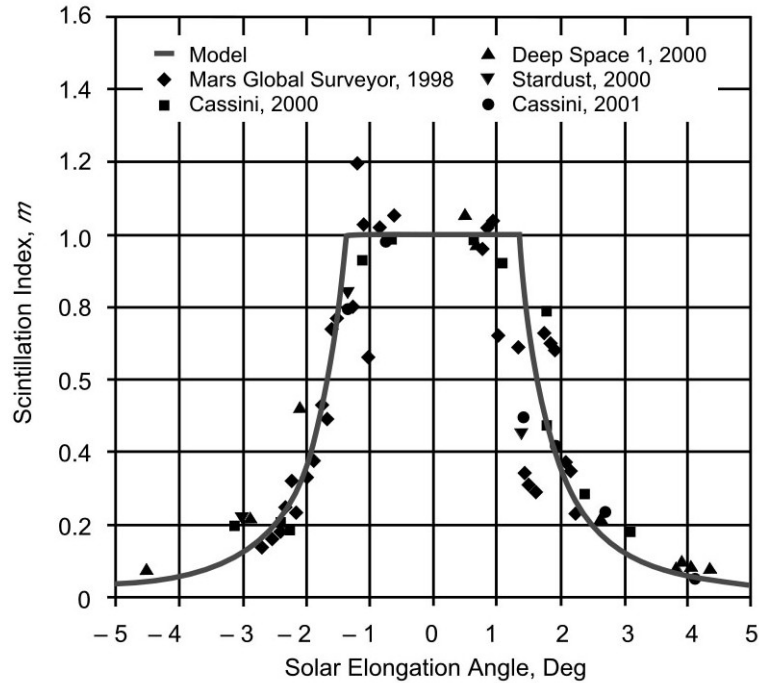


Figure 5. X-band Scintillation Index vs. Solar Elongation Angle.

The solar maximum scintillation observations of the Cassini 2000, Cassini 2001 and DS1 2000 solar conjunctions tend to be elevated with respect to the MGS 1998 data points, except during the solar events or streamer transits during egress.

#### 2.2.1.4 Discussion of the Ka-band Scintillation Measurements

The Ka-band scintillation measurements provide a reasonably good match to the theoretical model as seen in Figure 6. In addition to there being less scintillation at Ka-band relative to X-band for the same SEP angle, there is also less variability in the Ka-band scintillation index measurements, although it is cautioned to keep in mind that the Ka-band data set lacks a sufficient number of measurements. The Ka-band curve appears to transition from weak scintillation to saturation near  $0.6^\circ$ .

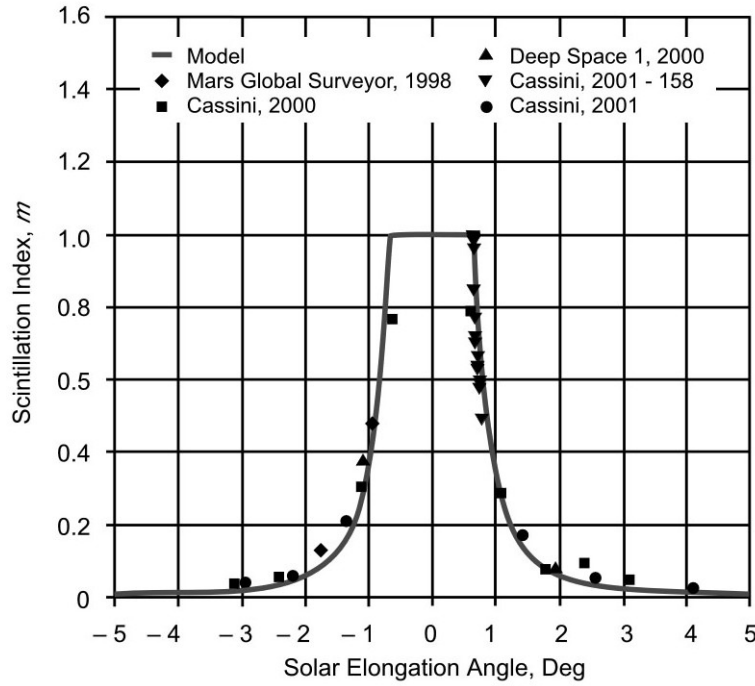


Figure 6. Ka-band Scintillation Index vs. Solar Elongation Angle.

A very few Ka-band data points were available from the MGS 1998 solar conjunction so the Ka-band data set is not as comprehensive as the X-band set. Changes in Ka-band scintillation index during the Cassini May 2000 solar conjunction were difficult to measure as the spacecraft was using thrusters to maintain pointing [8]. This caused signal amplitude excursions of as much as 20 dB with time scales on the order of 40 minutes. To minimize these effects for the Cassini May 2000 solar conjunction passes, the scintillation index for Ka-band was computed only during a short period of relatively constant signal strength – where dead-banding effects were minimal. The Cassini June 2001 solar conjunction used reaction wheel attitude control that provided excellent received signal strength stability.

#### 2.2.1.5 Scintillation Model

A complex model based on theoretical considerations has been developed and is presented in Reference [6]. A simplified, exponential/polynomial approximation to this theoretical model is provided as equation (7) and is shown as the solid curve in Figures 5 and 6.

$$m = \begin{cases} \exp[-a_1(|\theta| - \theta_t)] + a_2 + a_3(|\theta| - \theta_t) + a_4(|\theta| - \theta_t)^2, & (|\theta| - \theta_t) \geq 0 \\ 1, & (|\theta| - \theta_t) < 0 \end{cases} \quad (7)$$

In this model,  $a_1$ ,  $a_2$ ,  $a_3$ , and  $a_4$  are solve-for coefficients,  $\theta$  is the actual SEP angle, and  $\theta_t$  is near the SEP angle at which the scintillation index transitions to saturation ( $m = 1$ )

For X-band, the best-fit coefficients using the exponential model in (7) fit to the data with  $\theta_t = 1.35^\circ$  and  $|\theta_t| < 5^\circ$ . were:

$$\begin{aligned}a_1 &= 2.0 \\a_2 &= 0.14 \\a_3 &= -0.03 \\a_4 &= 0.0\end{aligned}$$

For Ka-band, the best-fit coefficients using the exponential model of (7) were:

$$\begin{aligned}a_1 &= 4.0 \\a_2 &= 0.07 \\a_3 &= -0.25 \\a_4 &= 0.002\end{aligned}$$

where  $\theta_t = 0.68^\circ$  and  $|\theta_t| < 5^\circ$ .

### **2.2.2 Spectral Broadening**

Spectral broadening of the received carrier signal occurs due to Doppler shifting of the charged-particle refractive index (or density) irregularities as they are carried over the signal path by the solar wind. It is dependent on both electron density fluctuations and solar wind velocity, whereas the scintillation index only depends on the electron density fluctuations. Spectral broadening is observed when the signal path passes close enough to the Sun such that the broadening exceeds the line width of the spacecraft oscillator. Oscillator line widths are typically  $<0.02$  Hz for ultra-stable oscillators (USOs) and  $<3$  Hz for auxiliary oscillators. The broadened bandwidth,  $B$ , can be observed with the Radio Science Receiver (see module 209) and is defined as the bandwidth in which half of the carrier power resides.

Spectral broadening is not normally of concern in designing a telemetry link because it does not become significant until the SEP angle becomes so small that the telemetry performance has already become degraded due to intensity scintillation effects. However, it is of concern to a telecommunications engineer to determine an adequate value for the ground receiver carrier tracking loop bandwidth. If the broadening is excessive, the tracking loop bandwidth will need to be widened in order to capture all of the frequency fluctuations but not so wide that receiver lock might be lost due to excessive thermal noise.

For Ka-band,  $B$  is below 1 Hz for SEP angles greater than 0.7 degrees. Since Ka-band ground tracking loop bandwidths are usually set from 5 to 10 Hz, spectral broadening is not an issue considering that PSK telemetry is expected to degrade somewhere between 0.7 and 1.0 degrees SEP angle due to increased intensity scintillation destroying phase knowledge. Below 0.7 degrees, Ka-band  $B$  has been known to reach values of approximately 2 Hz at an SEP angle near 0.6 degrees.

For X-band,  $B$  usually lies below 2 Hz for SEP angles greater than 1 degree and below 1 Hz for SEP angles greater than 2 degrees. As is the case with Ka-band, telemetry will become degraded before an SEP of 2 degrees is reached and spectral broadening becomes an issue. Below 1 degree, X-band  $B$  has been known to reach 14 Hz at an SEP angle near 0.6 degrees.

### **2.3            *Communications Strategies***

Standard downlink BPSK link design and coding strategies can be used to achieve successful X-band data return at SEP angles down to at least 2.3 degrees and similar success should be achievable at Ka-band down to an SEP angle of 1 degree. Solar effects are significantly reduced at Ka-band. The Ka-band carrier experiences 15 percent less amplitude scintillation and 20 percent less spectral broadening than the X-band carrier at the same SEP angle. The presence of solar events, the sub-solar latitude, and the phase of the solar cycle should also be considered in any strategy.

The use of one-way referenced links instead of two-way or three-way coherent links will result in links free of additional phase effects from the uplink signal. Any phase disturbance received by the spacecraft will be turned around by the spacecraft transponder and appear on the downlink (multiplied by the transponder ratio). The downlink will also incur its own phase scintillation as well as amplitude scintillation. For example, a Ka-band downlink using the spacecraft's Ultra-Stable Oscillator (USO) as the signal source will have significantly fewer solar effects than if the Ka-band downlink signal was referenced to the normal X-band uplink signal.

In regions of strong scintillations where conventional telemetry is likely to fail, it may be possible to provide notification of critical spacecraft events by the use of frequency semaphores with reasonable duration for integration and appropriate spacing in frequency. Non-coherent frequency-shift keying (FSK), although not presently supported by the DSN, may provide improved data return provided adequate link margin is available.



## ***Appendix A***

### ***References***

- 1 Berman, A. L. and Wackley, J. A., "Doppler Noise Considered as a Function of the Signal Path Integration of Electron Density," Deep Space Network Progress Report 42-33, March–April 1976," Jet Propulsion Laboratory, Pasadena, California, June 15, 1976
- 2 Muhleman, D, and Andeson, J., "Solar Wind Electron Densities from Viking Dual-frequency Radio Measurements," Astrophysical Journal, 247, 1093–1101, August 1, 1981
- 3 Bird, M., Volland, H., Patzold, M., Edenhofer, P., Asmar, S., and Brenkle, J., "The Coronal Electron Density Distribution Determined from Dual-frequency Ranging Measurement During the 1991 Solar Conjunction of the Ulysses Spacecraft," The Astrophysical Journal, 426, 373–381, May 1, 1994
- 4 Volland, H., Bird, M. K., Levy, G. S., Stelzreid, C. T., and Seidel B. L., "Helios-1 Faraday Rotation Experiment: Results and Interpretations of the Solar Occultations in 1975," Journal of Geophys. Research, 42, 659–672, 1977
- 5 Morabito, D. D., and Hastrup, R., "Communicating with Mars During Periods of Solar Conjunction" Proceedings of the 2002 IEEE Aerospace Conference, Big Sky, Montana, March 9-16, 2002.
- 6 Morabito, D.D. "Solar Corona Amplitude Scintillation Modeling and Comparison to Measurements at X-band and Ka-band. Interplanetary Network Directorate Progress Report 42-153, January–March 2003, pp. 1–14, May 15, 2003.
- 7 Morabito, D. D., Shambayati, S., Butman, S., Fort, D., and Finley, S., "The 1998 Mars Global Surveyor Solar Corona Experiment", The Telecommunications and Mission Operations Progress Report 42-142, April–May 2000, Jet Propulsion Laboratory, Pasadena, California, August 15, 2000.
- 8 Morabito, D. D., Shambayati, S., Finley, S., Fort, D., "The Cassini May 2000 Solar Conjunction," IEEE Transactions on Antennas and Propagation, Volume 51, No. 2, February 2003, pp. 201–219.
- 9 Morabito, D. D., Shambayati, S., Finley, S., Fort, D, Taylor, J. and Moyd, K., "Ka-band and X-band Observations of the Solar Corona Acquired During Solar Conjunctions of Interplanetary Spacecraft", Proceedings of the 7<sup>th</sup> Ka-band Utilization Conference, September 26, 2001, Santa Margherita Ligure, Italy. IIC - Istituto Internazionale delle Comunicazioni, Via Perinace - Villa Piaggio, 16125 Genova, Italy.
- 10 Feria, Y. Belongie, M. McPheeters, T. and Tan, H., "Solar Scintillation Effects on Telecommunication Links at Ka-band and X-band," The Telecommunications and Data Acquisition Progress Report 42-129, vol. January–March 1997. Jet Propulsion Laboratory, Pasadena, California, May 15, 1997.